Closer look at dark vector splitting functions in proton bremsstrahlung

S. Foroughi-Abari,[1,2,*] P. Reimitz,[3,†] and A. Ritz[2,‡]

[1]*Department of Physics, Carleton University, Ottawa, Ontario K1S 5B6, Canada*
[2]*Department of Physics and Astronomy, University of Victoria, Victoria, British Columbia V8P 5C2, Canada*
[3]*Instituto de Física, Universidade de São Paulo, 05508-090 São Paulo, SP, Brasil*

(Received 20 September 2024; accepted 4 July 2025; published 31 July 2025)

High luminosity colliders and fixed target facilities using proton beams are sensitive to new weakly coupled degrees of freedom across a broad mass range. Among the various production modes, bremsstrahlung is particularly important for dark sector degrees of freedom with masses between 0.5 and 2.0 GeV, due to mixing with hadronic resonances. In this paper, we revisit the calculation of dark vector production via initial state radiation in non-single-diffractive scattering, using an improved treatment of the splitting functions and timelike electromagnetic form factors. The approach is benchmarked by applying an analogous calculation to model inclusive ρ-meson production, indicating consistency with data from NA27 in the relevant kinematic range.

DOI: 10.1103/fzlm-gsd7

I. INTRODUCTION

The primary empirical motivations for new physics, in particular, the evidence for dark matter and neutrino mass, are relatively agnostic about the mass scale and so have motivated extensive efforts to explore scenarios that are light relative to the weak scale but necessarily weakly coupled [1–20]. This dark sector framework focuses on the small number of relevant or marginal interactions—i.e., the scalar, vector, and neutrino portals—that could connect an entirely neutral new physics sector to the Standard Model. Notably, the most interesting parameter range in these models is accessible to current and next generation high luminosity collider and fixed target facilities [21–59], for example, the mediator mass and interaction range required to explain models of thermal relic sub-GeV dark matter.

The evolving maturity of accelerator-based probes of dark sectors has highlighted the relative advantages of proton and electron beam facilities, with future development in the former case bolstered, for example, by the developing long and short baseline neutrino physics program at Fermilab [60,61], and the near-term opportunities for fixed target experiments such as SHiP in the CERN North Area [62], and forward physics detectors at the HL-LHC [63]. This motivates careful analysis of all the relevant hadronic production modes and detection strategies [64–70]. One of the most complex regimes involves the production of dark sector states of 0.5–2.0 GeV mass, where enhancement via resonant hadronic mixing is important. This mechanism is particularly advantageous for proton beam facilities where, in the forward region, and given the relatively low momentum transfer, it can be understood as proton bremsstrahlung. Conventional parton-level calculational approaches, e.g., for Drell-Yan, are not currently well suited for the production of sub-GeV mass states in the far forward region (very low Bjorken x). While radiative decays of final state hadrons provide the dominant production mode for dark sector masses below 0.5 GeV, approaches to the 0.5 to 2.0 GeV range have necessarily focused on coherent radiation from beam protons.

The underlying process of interest involves inclusive production of a dark state via proton beam collisions $p + p/n \to D + \cdots$ where D is a dark sector state. Such a bremsstrahlung-like process can be characterized via three subprocesses, $\text{Brem} \sim \text{ISR} + \text{FSR} + \text{Collective}$, comprising initial and final state radiation and collective effects in the underlying hadronic collision. Our focus here is on initial state radiation (ISR) in proton-proton scattering, as it is well defined given specified initial states. We revisit data-driven approaches to the calculation of this rate for dark vectors, specifically, kinetically-mixed dark photons, and explore and benchmark these contributions by comparing to the data on inclusive rho production. Initial approaches to proton bremsstrahlung generalized the successful Fermi-Weizsacker-Williams (WW) approximation for electron bremsstrahlung [32–34]. While this can be

*Contact author: saeidf@physics.carleton.ca
†Contact author: peter@if.usp.br
‡Contact author: aritz@uvic.ca

Published by the American Physical Society under the terms of the Creative Commons Attribution 4.0 International license. Further distribution of this work must maintain attribution to the author(s) and the published article's title, journal citation, and DOI. Funded by SCOAP³.

straightforwardly applied for quasielastic $pp \to ppV$ radiation, additional assumptions are required to extend this to the most relevant regime of inelastic scattering with a complex final state. In [71], several approaches to proton bremsstrahlung were studied, including pomeron-exchange models of ISR + FSR for quasielastic radiation, the hadronic WW approximation to quasielastic scattering, and an approach following Altarelli-Parisi to ISR in inelastic scattering referred to as the quasireal approximation (QRA). The latter approach provided a dominant contribution to the total rate, but the approximation leads to some unphysical features in the kinematic distributions, particularly for small vector mass. Indeed, for dark photon radiation, only the full combination of all initial and final state radiative processes will be manifestly gauge invariant. Nonetheless, for generic inelastic scattering, ISR should be a well-defined subprocess. Thus, our focus will be on carefully removing or suppressing any possible unphysical contributions. In this paper, we will address these issues and also provide a more comprehensive analysis of the form factors at the ISR proton vertex. Our final results for the ISR production rate for dark vectors at colliders with sample beam energies of 400 GeV and 14 TeV are shown in Fig. 5.

The remaining sections of this paper are organized as follows. Section II discusses the ISR approximation and the approach to determine a consistent splitting function for the production of a dark vector in proton-proton collisions. We improve on prior work by adopting the Dawson correction to maintain gauge invariance in the massless vector limit. Section III presents a more precise ppV form factor in the timelike region, based on data for the Pauli and Dirac proton electromagnetic form factors. The ensuing production rates and kinematic distributions are presented in Sec. IV, along with an application of the QRA approach to inclusive rho production, allowing for a comparison to data as a benchmark. Further technical details on the form-factor parametrizations are covered in Appendix A, with fits provided in the Supplemental Material [72] for ease of implementation. Section V contains a brief discussion of the results and prospects for further improvements in precision.

II. ISR SPLITTING FUNCTIONS

This analysis will focus on new dark sector degrees of freedom coupled to the Standard Model via the vector portal, and thus the initial state radiation of dark photons A', defined via kinetic mixing with photons, or, equivalently, their coupling to the electromagnetic current $J^\mu_{\rm EM}$,

$$\mathcal{L} = -\frac{1}{2}\epsilon F^{\mu\nu}F'_{\mu\nu} = -\epsilon e J^\mu_{\rm EM} A'_\mu. \tag{1}$$

This coupling allows us to infer the coupling of A' to nucleons (and we focus here on protons), which we later parametrize by taking into account both monopole and dipole form factors; however, in this section we retain just the constant charge coupling for simplicity.

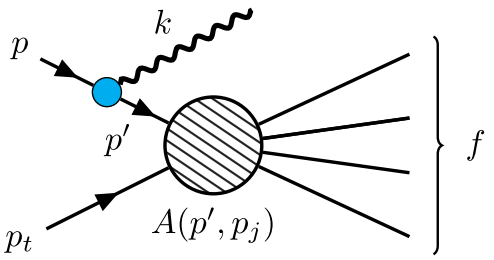


FIG. 1. Dark sector initial state radiation in a generic non-diffractive scattering event.

Following [71], we focus on the dominant bremsstrahlung contribution coming from ISR in non-single-diffractive (NSD) collisions. While ISR and FSR interfere in quasielastic and single diffractive processes [71], they are intrinsically decoupled in fully inelastic collisions, where the final state is more complex. For a comparison between ISR in NSD collisions, as presented in this paper, and the treatment of ISR + FSR in the WW approximation, we refer to [71].

To analyze ISR in NSD scattering, we use an on-shell approach [73–77], namely, the quasireal approximation discussed in [71], to factorize the differential cross section for initial state radiation into a calculable splitting probability and the underlying non-single-diffractive proton-proton interaction cross section for which a fit to data is readily available.

The amplitude is represented schematically in Fig. 1, with a vector radiated from the incoming "beam" proton p with momentum p_p, which then undergoes inelastic scattering with the "target" proton p_t with amplitude $A(p' = p - k, p_j)$. Here k is the momentum of the radiated dark vector, and p_j denotes the momenta of the other particles involved in the inelastic process. In the high-energy limit, the quasireal approximation represents the intermediate proton propagator using an on-shell polarization sum, so the matrix element takes the form [71]

$$\mathcal{M}_r^{pp_t\to Vf}(p,k,p_j) \approx \sum_{r'} \mathcal{M}_{r'}^{pp_t\to f}(p-k,p_j)\left(\frac{V_{r'r}}{2k\cdot p - m_V^2}\right), \tag{2}$$

with the vertex function $V_{r'r,\lambda} = \epsilon e \bar{u}^{r'}(p')\not{\epsilon}^\star_\lambda(k)u^r(p)$.

For concreteness, we now specify the momenta in the infinite momentum frame,

$$p^\mu = \left(p_p + \frac{m_p^2}{2p_p}, \mathbf{0}, p_p\right), \tag{3}$$

$$k^\mu = \left(zp_p + \frac{p_T^2 + m_V^2}{2zp_p}, \mathbf{p}_T, zp_p\right), \tag{4}$$

$$p'^{\mu} = \left((1-z)p_p + \frac{p_T^2 + m_p^2}{2p_p(1-z)}, -\mathbf{p}_T, (1-z)p_p\right), \quad (5)$$

where z is the fraction of the longitudinal momentum carried by the dark photon with transverse momentum $\mathbf{p}_T$. Integrating over the phase space of the remaining particles in the final state f following [71], the ISR cross section can then be factorized as follows,

$$d\sigma^{pp_t\to Vf}(s) \approx d\mathcal{P}_{p\to p'V} \times \sigma_{pp}^{\mathrm{NSD}}(s'). \quad (6)$$

Here we have introduced the differential splitting probability $d\mathcal{P}_{p\to p'V}$ and retained only the NSD cross section $\sigma_{pp}^{\mathrm{NSD}}(s')$, parametrized following Ref. [78] as

$$\sigma_{\mathrm{NSD}}(s) = 1.76 + 19.8\left(\frac{s}{\mathrm{GeV}^2}\right)^{0.057} \mathrm{mb}, \quad (7)$$

since radiation in single diffractive processes is suppressed by ISR and FSR interference [71]. After accounting for the momentum of the emitted dark vector, the underlying hadronic cross section is a function of $s' \simeq s(1-z)$, where this approximation is valid up to very large z or large angles, beyond which it must be replaced with a complete p_T-dependent expression.

The differential splitting probability can be represented in the form

$$d\mathcal{P}_{p\to p'V} \equiv w(z, p_T^2) dz dp_T^2 = \left(\frac{1}{16\pi^2 z}\frac{|\overline{\mathcal{M}_{p\to p'V}}|^2}{((p-k)^2 - m_p^2)^2}\frac{E_{p'}}{E_p}\right) dz dp_T^2, \quad (8)$$

where $|\overline{\mathcal{M}_{p\to p'V}}|^2 \equiv \frac{1}{2}\sum_{\mathrm{spin,pol}} V_{r',r,\lambda} V^{\star}_{r'',r,\lambda}$, and we have introduced the splitting function $w(z, p_T^2)$, which will be the primary quantity for the following discussion.

The validity of this factorized approximation to the ISR process relies on kinematic conditions, including that the off-shell momentum of the intermediate proton should be small relative to scales in the hard scattering and that the beam energy should be the dominant kinematic quantity. As discussed in [71], we require that (i) $(p'^2 - m_p^2) \ll 4(1-z)^2 p^2$, (ii) $p_T, m_p(m_V) \ll E_p(E_k)$, and (iii) an off-shell form factor is introduced to control the $pp'V$ vertex as detailed below.

A. Effective QRA splitting function

Direct calculation, summing over all helicities using the vertex functions above and on-shell polarization vectors, leads to the splitting function [71]

$$w_1(z, p_T^2) = \frac{\alpha\epsilon^2}{2\pi H}\left[z - z(1-z)\left(\frac{2m_p^2 + m_V^2}{H}\right) + \frac{H}{2zm_V^2}\right], \quad (9)$$

where we have set form factors to unity for the moment and introduced the kinematic structure function $H(z, p_T^2) \equiv p_T^2 + z^2 m_p^2 + (1-z)m_V^2$.

Although this result has a number of the anticipated scaling relations in the relevant kinematic limits, it was noted in [71] that it exhibits an unphysical $1/m_V^2$ singularity as $m_V \to 0$, due to the longitudinal polarization of the vector. This unphysical mass dependence in the splitting function is also observed at the parton level, e.g., within the electroweak $q \to q'V$ splitting functions used in HERWIG. The $m_V \to 0$ divergence caused by the longitudinal vector mode was highlighted in [79], which utilized the effective vector approach of Dawson to remove the part of the longitudinal polarization that is proportional to the four-momentum [80]. We now explore the use of this procedure for the QRA splitting function.

The contribution related to the longitudinal polarization $\varepsilon_L(k)$ proportional to the four-momenta k^{μ} of the massive spin-1 vector gives zero when sandwiched between fermion spinors $\bar{u}^r(p')\not{\varepsilon} u^s(p) \to \bar{u}^r(p')\not{k} u^s(p) = 0$, where p and $p' = p - k$ denote the four-momenta of the incoming and outgoing fermions, respectively, and we used the equation of motion. Thus, one can neglect terms proportional to k, and it is sufficient to use

$$\varepsilon_0^{\mu}(k) \equiv \varepsilon_L^{\mu}(k) - \frac{k^{\mu}}{m_V} = \frac{m_V}{(k_0 + |\vec{k}|)}(-1, \vec{k}/|\vec{k}|). \quad (10)$$

The polarization sum, including the transverse contribution $\sum_{i=1,2,L} \varepsilon_i^{\mu}(k)\varepsilon_i^{\nu\star}(k) = -g^{\mu\nu} + \frac{k^{\mu}k^{\nu}}{m_V^2}$, can then be written using Eq. (10) as

$$\sum_{i=0,1,2} \varepsilon_i^{\mu}(k)\varepsilon_i^{\nu\star}(k) = -g^{\mu\nu} - \frac{k^{\mu}\varepsilon_0^{\nu} + \varepsilon_0^{\mu}k^{\nu}}{m_V}. \quad (11)$$

In our treatment of the splitting vertex, we consider the outgoing intermediate proton to be on shell. This necessitates forcing the condition p' to be on shell in the spinor sandwich such that the intermediate proton's three-momentum is fixed, $\vec{p'} = \vec{p_p} - \vec{k}$, while the energy is not automatically conserved at the $pp'V$ vertex, i.e., $E_{p'} \neq E_p - E_k$. This in turn gives $p' = p - k + \delta$ with $\delta^{\mu} = (H/2z(1-z)p_p, \vec{0})$, where we used the momenta defined in the infinite momentum frame, Eq. (3).

Using the modified polarization sum in Eq. (11), the effective splitting function takes the form

$$w_1^{\mathrm{eff}}(z, p_T^2) = \frac{\alpha\epsilon^2}{2\pi H}\left[\frac{1 + (1-z)^2}{z} - z(1-z)\left(\frac{2m_p^2 + m_V^2}{H}\right)\right], \quad (12)$$

which exhibits smooth behavior in the massless limit and resembles the Altarelli-Parisi splitting kernel of the SM photon. Indeed, this splitting function ensures that the

production rate satisfies the scaling relation $d\sigma/dk \propto 1/k$ in the massless vector limit, consistent with the soft photon theorem [81–83]. In practice, ISR itself is not expected to provide a good approximation for soft radiation in the massless limit, as the quasielastic process requires consistent treatment of FSR. Indeed, we have verified that both the pomeron-exchange approach to quasielastic $pp \to ppV$ radiation and the hadronic WW approximation to this quasielastic approach, which were discussed in detail in [71], satisfy the soft theorem with the required coefficient. Nonetheless, the approach above proves practical for analyzing radiation of sufficiently massive vectors in inelastic scattering.

The correction leading to the effective splitting function (12) can be understood as prioritizing gauge invariance at the ISR vertex but at the cost of slightly violating energy conservation within the QRA scheme. In particular, the impact of dropping terms proportional to $p - p'$ in ϵ_L^μ is a correction to the splitting function w_1 that takes the form $(\frac{H}{2zm_V^2} - \frac{2(1-z)}{z})$ and naturally diverges as $m_V \to 0$. This impacts the on-shell condition for the intermediate proton within QRA, but fortunately, energy conservation is controlled by the form factor $F_{pp'V}(p'^2)$ discussed in the next section.

B. Comparison to WW approaches

The conventional WW approximation as applied successfully to model bremsstrahlung in electron scattering cannot be applied directly to radiation in inelastic scattering, due to the generic nature of the final state. However, a prescription to apply the splitting function obtained in the WW approximation to quasielastic scattering was proposed initially in [32] and adopted in a number of subsequent phenomenological analyses. This approach follows the parametrization of the differential ISR rate given in (6), using the total inelastic pp scattering cross section $\sigma_{pp}^{\rm tot}$ [32],

$$\left(\frac{d\sigma_{pp\to Vf}^{\rm inel}}{dz dp_T^2}\right)_{\rm Mod\,WW} \equiv w_1^{\rm WW}(z, p_T^2) \times \sigma_{pp}^{\rm tot}(s'), \tag{13}$$

where $w_1^{\rm WW}$ is an effective splitting function that appears within the WW approach to quasielastic scattering, with radiation from initial and final state protons,

$$\begin{aligned} w_1^{\rm WW}(z, p_T^2) = \frac{\alpha\epsilon^2}{2\pi H}\Bigg[&\frac{1+(1-z)^2}{z} \\ &- 2z(1-z)\left(\frac{2m_p^2+m_V^2}{H} - z^2\frac{2m_p^4}{H^2}\right) \\ &+ 2z(1-z)(1+(1-z)^2)\frac{m_p^2 m_V^2}{H^2} \\ &+ 2z(1-z)^2\frac{m_V^4}{H^2}\Bigg]. \end{aligned} \tag{14}$$

This function will be discussed further below, and we refer to this prescription [32] as the modified WW approach in providing comparisons. It is notable that the first two terms in the quasielastic splitting function (14) agree with the effective QRA splitting function in (12) apart from an additional factor of 2 in front of the second term. This difference and the terms quartic in mass in (14) reflect its origin in the two WW subprocesses for ISR + FSR in quasielastic scattering [32].

It is helpful to compare the above approach with a direct calculation of quasielastic radiation in elastic scattering, $p + p \to p + p + V$. This ISR + FSR combination was computed in [71] via both an explicit calculation using pomeron exchange and a straightforward hadronic generalization of the WW approximation used for electron beams, with both approaches agreeing well (see also [84] for a recent analysis). Importantly, it was observed that the ISR + FSR combination showed substantial interference, with the resulting rate being substantially lower than either ISR or FSR alone. Due to the more complex final state, this interference is not expected to apply to ISR for non-single-diffractive scattering. As the quasielastic rate combines both ISR + FSR, we simply define an effective splitting function as follows,

$$w^{\rm elastic}(z, p_T^2, s) \equiv \frac{1}{\sigma_{pp}^{\rm el}(s)}\frac{d\sigma_{pp\to ppV}^{\rm el}}{dz dp_T^2}, \tag{15}$$

where $\sigma_{pp}^{\rm el}$ is the elastic scattering cross section and $w^{\rm elastic}$ can be compared numerically to the ISR splitting functions.

To explore this further, we note that the hadronic WW approach provides a good approximation to (15) in this regime and can be represented analytically in terms of the splitting function $w_1^{\rm WW}$ [71],

$$\left(\frac{d\sigma_{pp\to ppV}^{\rm el}}{dz dp_T^2}\right)_{\rm WW} \approx w_1^{\rm WW}(z, p_T^2)\frac{z^2}{H}\left(\frac{\chi}{4\pi}\right), \tag{16}$$

where χ reflects the factorized dependence on the underlying elastic scattering cross section,

$$\frac{\chi}{4\pi} = \int_{t_{\rm min}}^{t_{\rm max}} dt(t - t_{\rm min})\frac{d\sigma_{pp}^{\rm el}}{dt}, \tag{17}$$

with $t_{\rm min} \approx -H^2/(2z(1-z)p_p)^2$ and $t_{\rm max} \approx -2(1-z)m_p p_p$. The WW splitting function is defined in this case by $w_1^{\rm WW}(z, p_T^2) = (\alpha\epsilon^2/2\pi H)(1-z)/2z\mathcal{A}^{2\to 2}_{t=t_{\rm min}}$ and can be reexpressed in the form given in (14), using the expression $\mathcal{A}^{2\to 2}_{t=t_{\rm min}} = 2(1+(1-z)^2)/(1-z) - 4z^2 p_T^2(2m_p^2 + m_V^2)/H^2$ for the squared amplitude for the WW 2 to 2 subprocess of 2 to 3 quasielastic scattering [85].

It is notable that while both the direct and WW computations of this quasielastic scattering rate in [71] utilized the model of pomeron exchange for the underlying

process of proton-proton scattering, the splitting probability itself is quite robust to the choice of underlying interaction model. As shown recently in [84], an analogous WW approach, which instead utilizes massless vector propagators and vertices, leads to an almost identical result.

We will compare and contrast the differential distributions obtained using the effective QRA and modified WW approaches to ISR along with radiation in quasielastic scattering after discussing the important role played by form factors.

III. FORM FACTORS

Coherent emission of a dark vector with timelike momentum from a composite state such as a proton requires the introduction of form factors that depend on at least two invariants k^2 and p'^2 due to the intermediate proton nominally being off shell. In practice, the QRA formalism requires that p' not be too far off shell for overall energy conservation. We will parametrize the form factors as follows [71],

$$F_i(t, p'^2) = \mathcal{K}_{pp'V}(p'^2) \times F_i(t) \tag{18}$$

where $F_i(t = k^2)$, for $i = 1, 2$, denotes the conventional on-shell electromagnetic form factors for the proton, while $\mathcal{K}_{pp'V}$ controls the off-shell behavior of the intermediate proton line. This function plays an important role within the QRA approach in filtering out potentially unphysical kinematic contributions due to the lack of precise energy conservation at the dark vector vertex. This implies that $\mathcal{K}$ has the role of a "kinematic filter" within the QRA formalism, which goes beyond the normal expectation of simply accounting for compositeness in the off-shell proton. For this reason, rather than pursuing a more physical approach, adopted, e.g., by Davidson and Workman [86,87] where issues of gauge invariance can also be addressed, we model $\mathcal{K}$ via a simple dipole form [71],

$$\mathcal{K}_{pp'V}(p'^2) = \frac{1}{1 + (p'^2 - m_p^2)^2/\Lambda_p^4}, \tag{19}$$

with a sliding scale Λ_p controlling the level of off-shell contributions. The impact of this form factor is most easily understood by considering the rest frame of the emitting beam proton $p \to p' + V$. The form factor limits the off shellness of p' so that all kinematic scales are small ($\sim m_p$) in this frame, while in the lab frame the momentum of V approaches $E_{\rm beam}/2$. Thus, in considering small V momentum, p' is necessarily more off shell, and the form factor suppresses the rate. This effect becomes less significant as the V mass is lowered below the hadronic scale, and indeed, the effect of the form factor is negligible for radiating soft (massless) photons.

Turning now to the electromagnetic form factors $F_i(t)$, we extend earlier work by defining the coupling to nucleons in the standard manner, taking into account both electric (Coulomb) and magnetic (spin-flip) interactions,

$$\langle N|J^\mu_{\rm em}|N\rangle = \bar{u}(p')\left[\gamma^\mu F_1^N(t) + \frac{i\sigma^{\mu\nu}(p'-p)_\nu}{2m_N} F_2^N(t)\right]u(p), \tag{20}$$

where $k = p - p'$ and $t = k^2$ is timelike for the ISR vertex. The $p \to p'V$ vertex function is then generalized accordingly, and evaluating $|\overline{\mathcal{M}_{p\to p'V}}|^2$ with the Dawson-corrected polarization of Eq. (11), we obtain

$$\begin{aligned} w_F(z, p_T^2) = {} & w_1^{\rm eff}(z, p_T^2)|F_1(k^2, p'^2)|^2 \\ & + w_2^{\rm eff}(z, p_T^2)|F_2(k^2, p'^2)|^2 \\ & + w_{12}^{\rm eff}(z, p_T^2){\rm Re}[F_1(k^2, p'^2)F_2^\star(k^2, p'^2)], \end{aligned} \tag{21}$$

where $w_1^{\rm eff}$ is the splitting function given earlier in (12), and

$$\begin{aligned} & w_2^{\rm eff}(z, p_T^2) - w_1^{\rm eff}(z, p_T^2) \\ & = \frac{\alpha\epsilon^2}{4\pi m_p^2}\left[1 - (1-z)\left(\frac{4m_p^2 + m_V^2}{H}\right)\right] \\ & \quad \times \left[\frac{1}{z} - \frac{1}{4}z\left(\frac{4m_p^2 - m_V^2}{H}\right)\right], \\ & w_{12}^{\rm eff}(z, p_T^2) = \frac{\alpha\epsilon^2}{2\pi H}\left[2z - z(1-z)\frac{3m_V^2}{H}\right]. \end{aligned} \tag{22}$$

Information about the Sachs parametrization of the form factors $G_E(t) = F_1(t) + t/(4m^2)F_2(t)$ and $G_M(t) = F_1(t) + F_2(t)$ (and thus the Dirac and Pauli form factors) is primarily obtained through measurements of $\sigma(e^+e^- \to N\bar{N})$ in the physical timelike region and from $e^-p \to e^-p$ elastic scattering in the spacelike region. Subsequently, utilizing the normalization from the electric charge and magnetic moment and large t asymptotics from perturbative QCD (quark counting rules) as guidelines, an extended vector-meson dominance (VMD) model is employed to extrapolate further into the so-called unphysical region from $t = 0$ to $t = 4m_N^2$. Reference [88] utilized a minimal VMD model for the form factors with only ρ and ω resonances, assuming identical masses for ground states ($m_\rho = m_\omega = 0.770$ GeV) as well as for the excited states. In this paper, we explore a more elaborate resonance-based model, along with a modern dispersive approach for parametrizing nucleon electromagnetic form factors. The proton and neutron Pauli and Dirac form factors in the timelike region, as predicted by these models, are compared in Appendix.

We observe that the inclusion of a ϕ pole and continuum contributions to the isoscalar part of the form factor may

have a sizable impact on dark photon production predictions for masses in the GeV range. Although we expect direct ϕ-nucleon interactions to be highly suppressed according to the OZI rule [89–91], higher-order effects generate a non-negligible effective ϕNN interaction and an associated enhancement in the form factor around $\sqrt{t} \sim m_\phi \sim 1$ GeV. Indeed, as discussed in the dispersive analysis of [92], the isoscalar region around 1 GeV consists primarily of $\rho\pi$ and $K\bar{K}$ continuum contributions in addition to an intrinsic ϕ-meson pole that is damped due to cancelations. In contrast, the ω resonance is well isolated and prominent, making it possible to extract an ωNN coupling. Alternatively, the unitary-analytic (UA) model [93], which generalizes the approach of [88], contains just a series of neutral vector-meson poles within the framework of VMD [94–96]. This approach entails a clear peak structure in the form factors and gives much more significance to the ϕ pole as seen in Fig. 2. However, in this model, the overall height of the form factor in the relevant timelike region is somewhat lower than the dispersive result, as seen in Fig. 9. Thus, to be conservative we adopt the UA model to determine physical rates. Nonetheless, we note that both modeling approaches lead to a broad enhancement of the form factors above 1 GeV, relative to the simplified VMD model, due to the impact of broad resonances.

There are several possibilities to estimate the form factor uncertainty in the "unphysical region." The number of data points outside the unphysical region ensures that the uncertainty in the fit itself is rather small, but this does not account for the intrinsic uncertainty in the model, which is more important here as we wish to use the form factors in the unphysical timelike region. Indeed, the fit values are expected to be primarily sensitive to the region where the fit function is actually fitted to data. However, our interest lies in the hadronic resonance region with parameters fixed to their most recent PDG values [97]. Consequently, we focus on the intrinsic uncertainty in choosing the fit function parametrization and vary the resonance masses around their documented experimental uncertainty. We observe that the additional uncertainty in the widths, in particular, of heavier resonances, inflates the uncertainty bands significantly further and limits the confidence in the fit in that region (as indicated by dashed lines in our final production rates). Our final results for the form factors, utilizing the UA model, are shown in Fig. 2. Further details can be found in Appendix.

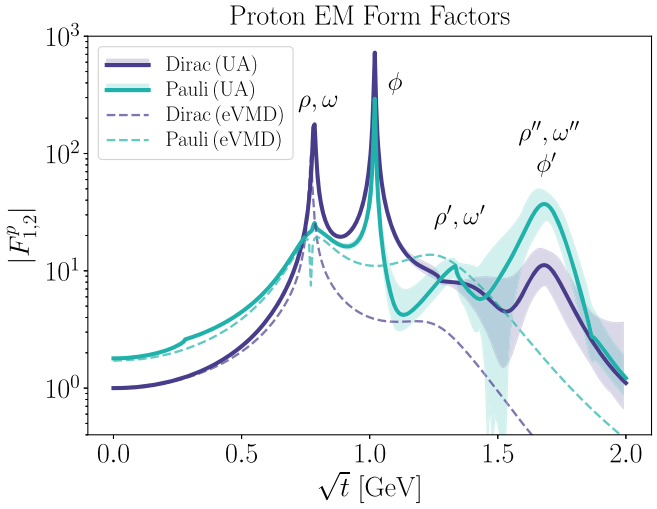


FIG. 2. Proton electromagnetic form factors in the timelike region based on the UA model [93], with fits provided in Ref. [72]. For comparison, dashed lines represent the simpler extended VMD (eVMD) model [33,88]. The meson labels indicate the approximate locations of the resonance structures, with $'$ and $''$ denoting the first and second excited resonance states, respectively. See the text for further details.

IV. PRODUCTION RATES AND BENCHMARKS

In this section, we present the final production rates and distributions using the effective QRA approximation for ISR, along with comparisons to other approaches. We also test the effectiveness of this approach within the Standard Model by using the corresponding ISR vertex with an off-shell photon to model the production of ρ-mesons via proton bremsstrahlung. This allows a direct comparison to inclusive ρ-production data from NA27 to benchmark the rate.

A. Dark vector production rates and distributions

We first illustrate the various differential distributions $d\mathcal{P}_{p\to p'V}$ for two different beam energies in Figs. 3 and 4. These panels help to clarify the impact of the off-shell form factor $\mathcal{K}$, while the EM form factors are not included to aid these comparisons.

It is instructive to compare the QRA approach to ISR with the well-defined computation for quasielastic scattering, which, for example, satisfies the correct scaling in the soft photon limit. It is apparent that the rate of the quasielastic process is suppressed when off shellness is large ($H/z \gg 1$). We observe that this feature is not apparent in the naive rates obtained using either QRA or the modified WW approximation. However, this feature is restored by including the off-shell form factor $\mathcal{K}$ for the intermediate proton line. Indeed, when the energy of the radiated massive state is low ($z \to 0$, $m_V \sim m_p$), the off-shell form factor applied to ISR scales as z^2, providing a corresponding suppression factor. A more precise comparison follows from the hadronic WW approximation to the quasielastic rate, as given in (16), $d\sigma/dz dp_T^2 \sim z^2 \times w_1^{\mathrm{WW}} \times \chi/(4\pi H)$. This can be approximated further in the regime where $H \sim m_p^2$, and to evaluate the integral expression for χ, we approximate the elastic cross section by a simple exponential falloff $d\sigma^{\mathrm{el}}_{pp}/dt \propto \exp(-B|t|)$, where the diffractive slope $B(s) \sim \mathcal{O}(10)$ mb [98]. This gives $\chi/4\pi \approx \sigma^{\mathrm{el}}_{pp}(s)/B(s) \sim \mathcal{O}(1)$ for $B|t_{\mathrm{min}}| \ll 1$,

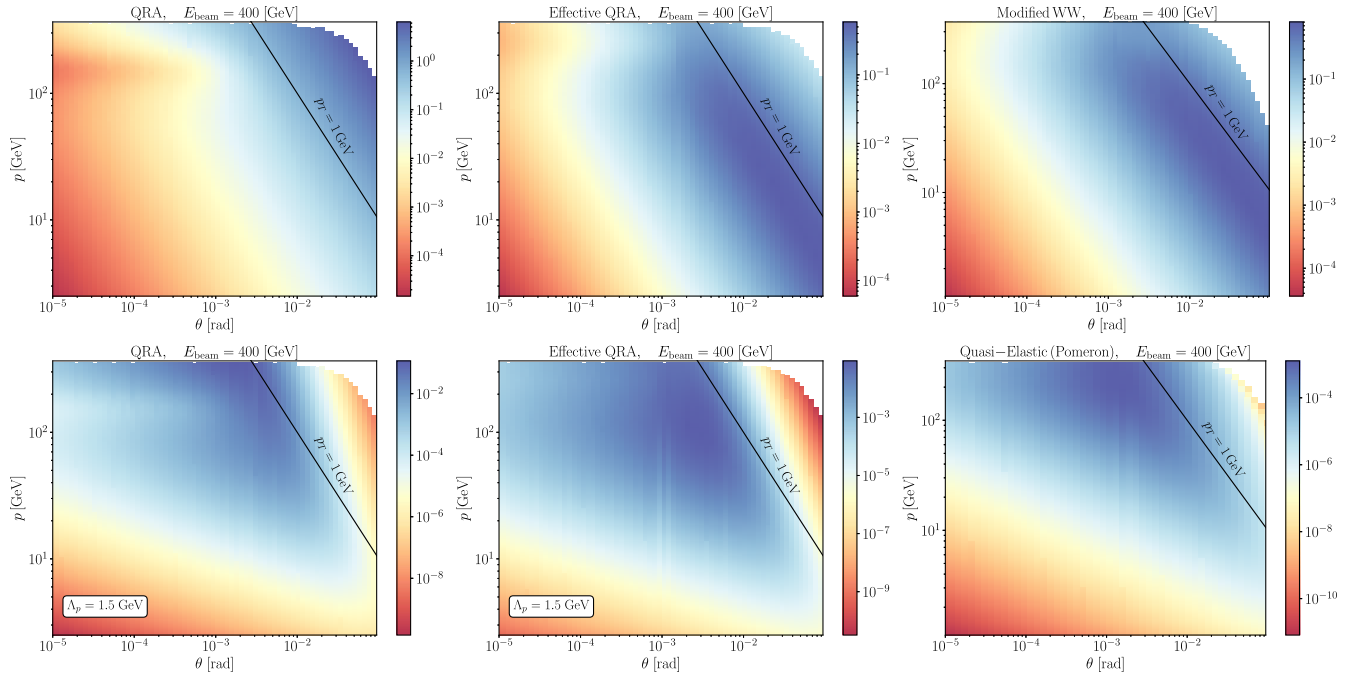


FIG. 3. Production distributions $d\mathcal{P}_{p\to p'V}$ for $m_V = 0.5$ GeV at a 400 GeV fixed target experiment shown for several approximations to proton bremsstrahlung, labeled QRA, effective QRA, modified WW, and quasielastic, as described in the text. The plots in the first two columns show the impact of the off-shell form factor $\mathcal{K}$ within the QRA and effective QRA approaches.

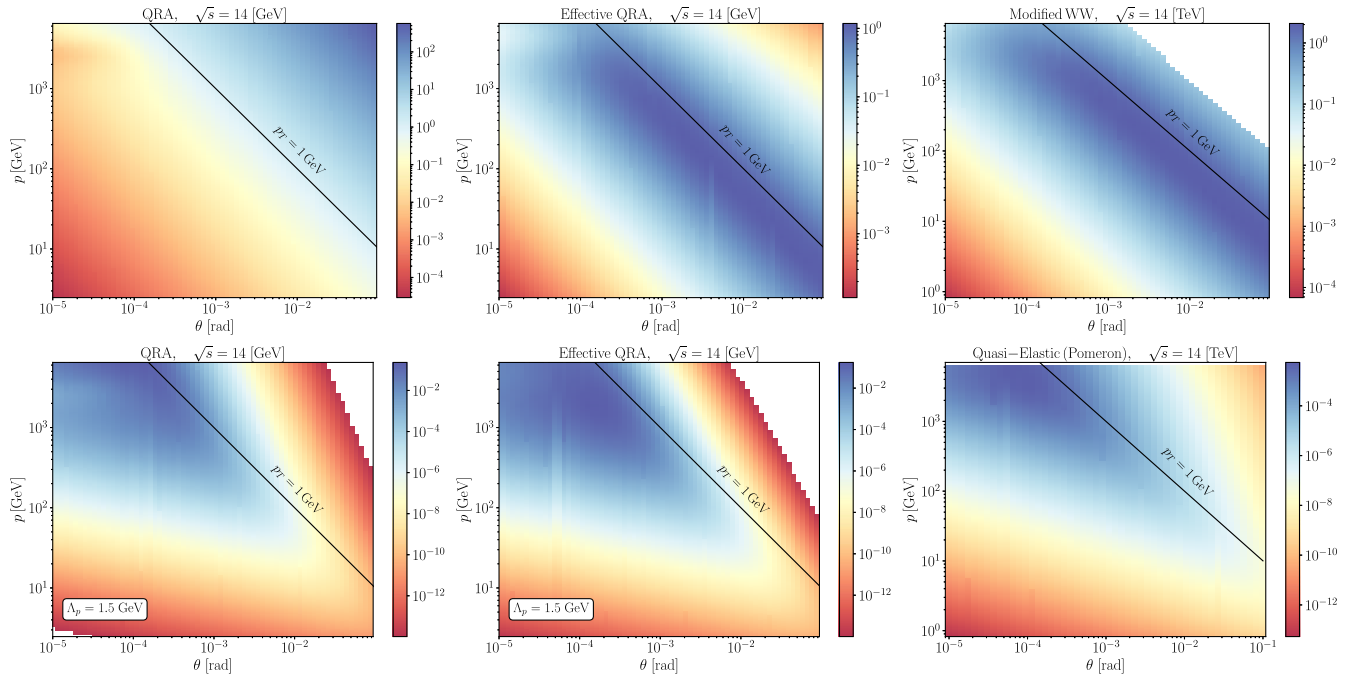


FIG. 4. Production distributions for $m_V = 0.5$ GeV in the center-of-mass frame at a forward LHC or HL-LHC experiment, shown for a variety of approximations to proton bremsstrahlung, following the same layout as Fig. 3.

so the scaling of the rate with z^2 is apparent. This kinematic feature helps to explain why the ISR distributions, when modulated by the off-shell form factor, exhibit a similar functional form to that for quasielastic scattering.

Another notable feature of the distributions is that the incorporation of the Dawson correction into the effective QRA approach removes an unphysical feature for small angles and large momenta that is observable in the QRA

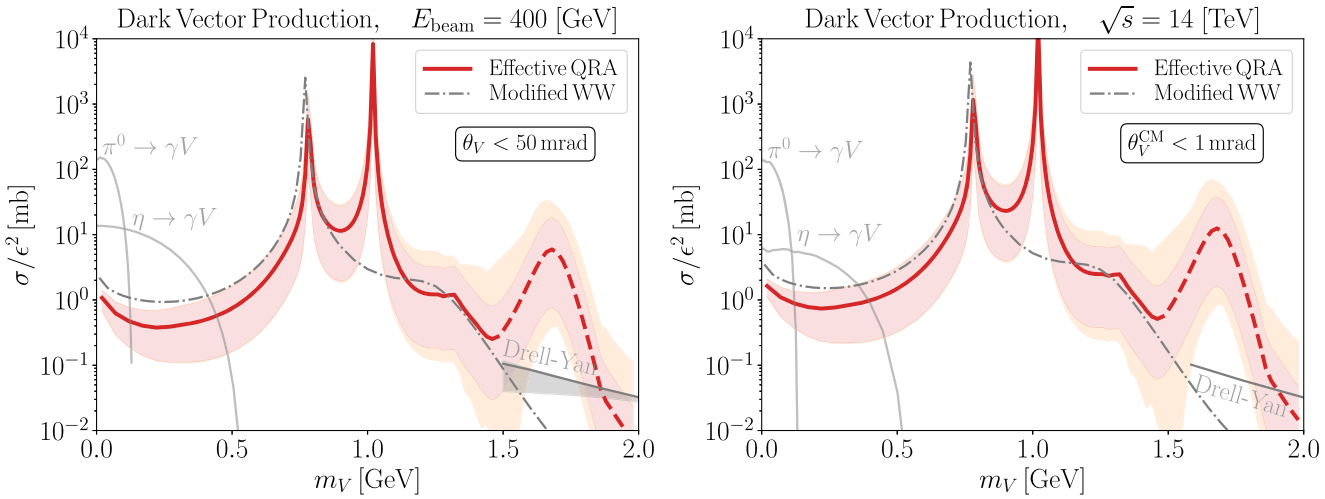


FIG. 5. Production cross section of dark vectors shown as a function of mass for (left) a 400 GeV fixed target beam, with an angular range of 50 mrad from the beam axis, and (right) at 14 TeV (center-of-mass) energy, within 1 mrad of the beam axis (center-of-mass frame). The improved quasireal approximation in non-single-diffractive scattering with a cutoff $\Lambda_p = 1.5$ GeV is shown in red. The red uncertainty band is represented by varying Λ_p within the interval [1, 2] GeV. Stacked on top in orange is an estimate of the uncertainty in the EM form-factor parametrization. The dashed gray curve employs the modified WW approach [32], utilizing the simpler VMD form factor, with a cut on transverse momentum $p_T < 1$ GeV [50]. Lighter gray curves depict other production channels, as labeled.

distributions. Overall, the consistency of the effective QRA distribution with that derived for quasielastic scattering adds confidence to the consistency of the approach.

With the distributions in hand, on incorporating the timelike EM form factors, we can determine the total production rate for vectors of a given mass, as shown in Fig. 5. This figure indicates the impact of resonant mixing with vector mesons, and the uncertainty bands are determined by varying the filter scale Λ_p, along with the uncertainty in the EM form factors. We emphasize that there are additional production modes, e.g., final state radiation, that are not yet incorporated into the modeling of dark vector rates.

B. Comparison to inclusive ρ-meson production

We now consider benchmarking the ISR differential rate in relation to data for inclusive light vector-meson production, focusing on $\rho(770)$.

Fits to the kinematic distributions observed in inclusive meson production, including the vector mesons, ρ, ω, etc., have been found to simplify via the use of the Feynman scaling variable $x_F \equiv p_\ell/p_{\rm max}$ defined in the center-of-mass frame, where p_ℓ is the longitudinal momentum carried by the produced meson and $p_{\rm max} \approx \sqrt{s}/2$ at very large scattering energies. An alternative scaling variable $x_R \equiv E/E_{\rm max}$ in the center-of-mass frame has also been found to extend the range of validity of scaling at subasymptotic energies. Following [99], an efficient parametrization of the differential production cross section may be presented as follows,

$$E\frac{d^3\sigma}{dp^3} = \frac{E}{\pi p_{\rm max}}\frac{d^2\sigma}{dx_F dp_T^2} \approx A\frac{(1-x_R)^\alpha}{x_R^\beta}(1+Cx_R)\exp(-Bp_T^2), \quad (23)$$

where the exponents α and β are fits to the data (conventionally presented in terms of the x_F variable [100]). At all energies, the p_T dependence out to ~2 GeV is well presented by the exponential form, where the measured value of the exponent is $B = 2.6 \pm 0.1$ GeV^{-2} for the inclusive $\rho^0(775)$ meson at 400 GeV beam energy [100]. Alternatively, the parametrization can be expressed by a similar variable, $x_0 \equiv p/p_{\rm max} = \sqrt{x_F^2 + p_T^2/p_{\rm max}^2}$ [101].

The best-fit parametrization for the differential cross section in Eq. (23) as a function of x_F was determined by comparison with data for inclusive ρ^0 production from the NA27 experiment with $\sqrt{s} = 27.5$ GeV. The resulting parametrization was observed to lie within the error bars, and a confidence band was generated by varying the fit parameters within their uncertainties, resulting in a range of $d\sigma/dx_F$ curves consistent with the data. By changing the variables, the corresponding best-fit momentum-angle distribution as a function of momentum p at a fixed angle is presented in Fig. 6, in which the gray band illustrates the uncertainty in the fit.

Features of the distribution (23) have been motivated on the basis of Regge or string models for meson formation, reflecting the hadronic composite nature of the ρ. Thus, the large momentum asymptotics, in particular, exhibiting a large suppression, are not expected to translate directly to

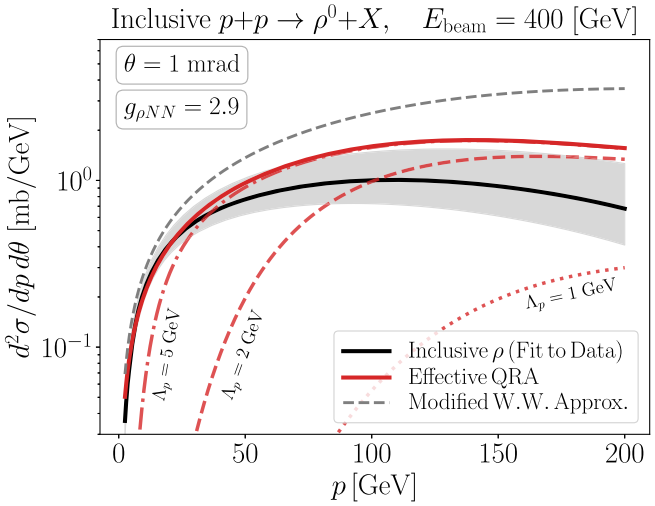


FIG. 6. Momentum-angle distributions for inclusive $\rho(770)$ meson production, comparing data from the NA27 experiment [100] (with a gray precision band) to the effective QRA and modified WW approaches. The choices of the Λ_p scale indicate the impact of the off-shell form factor in the effective QRA approach.

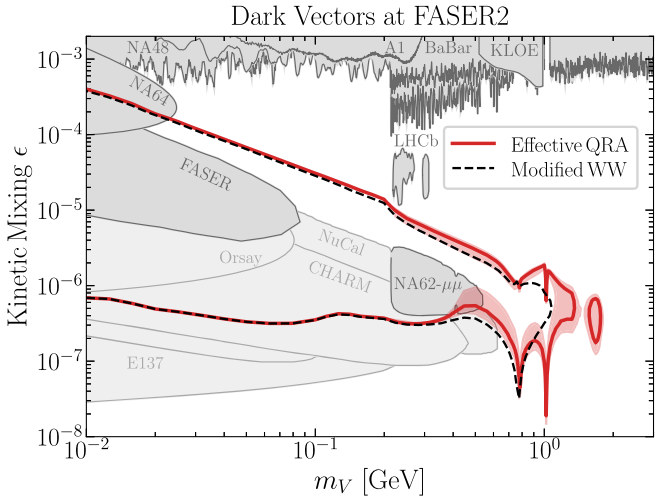


FIG. 7. Sensitivity reaches for dark vector decays at the FASER2 experiment, comparing bremsstrahlung production via the effective QRA (solid red) with the modified WW approximation (dashed black) with transverse momentum restricted to $p_T < 1$ GeV. This plot was created using the FORESEE [112] package. It incorporates various existing constraints along with the projections for FASER2, and it considers additional dark vector production modes.

the production of fundamental vectors such as dark photons. Nonetheless, a comparison for radiated momenta, which are small relative to the beam momentum, is informative as a test of models for proton bremsstrahlung and ISR, in particular. The fit refers to inclusive ρ production and thus necessarily incorporates modes beyond ISR or bremsstrahlung more generally. Accordingly, it can viewed as providing an approximate upper bound on the rate obtained by QRA or other mechanisms, at least for low momenta. To evaluate the production of neutral ρ mesons via the effective QRA approach, we use an effective ρ-nucleon vector coupling $\mathcal{L}_{\text{eff}} = g_{\rho NN}\bar{N}\gamma^\mu\vec{\rho}_\mu \cdot \vec{\tau}N$ with an average experimental value of $g_{\rho NN} = 2.9 \pm 0.3$ [102–104] and neglect the tensor coupling, having verified that its inclusion in the form $g_{\rho NN}\kappa_\rho/2m_N$ with $\kappa_\rho \sim 4$ [104] has a negligible effect. A comparison of the various calculational approaches with the fit to data from NA27 is shown in Fig. 6. Considering the kinematic regime with small longitudinal and transverse momentum, we observe similar behavior for the production rates from QRA, although the rate is suppressed by the off-shell form factor, while the modified WW approximation starts to exceed the rho production data for larger momenta. Importantly, Fig. 6 suggests that choosing a Λ_p scale around or slightly above the hadronic scale passes the test of not predicting an overproduction of ρ mesons in the relevant kinematic range.

C. Sensitivity to dark vectors

Finally, in this section, we illustrate the impact of the effective QRA production rate for proton bremsstrahlung on the sensitivity contours for the planned experiments SHiP and FASER2 in Figs. 7 and 8. These experiments are used as representative examples of searches at high-energy fixed target experiments and the HL-LHC, respectively. It is understood that there may also be impacts on the sensitivity at other existing or planned experiments (including NA62 [105,106], CHARM [107,108], NuCal [108,109], DarkQuest [110], FACET [111], etc.); however, our goal is simply to illustrate the impact of the model of ISR production, so we refrain from a more comprehensive analysis.

In the following, we summarize some of the experimental details relevant to dark photon searches:

(i) The Search for Hidden Particles (SHiP) experiment at the ECN3 High-Intensity Beam Facility [114] plans to deliver 6×10^{20} protons on a molybdenum alloy target as the hadron absorber. The experiment will utilize a muon shield that deflects muons from meson decay, creating an almost zero-background environment for searching for long-lived particles like dark photons. The Hidden Sector Decay Search (HSDS) detector, located about 33 meters from the target, features a 50-m-long vacuum decay vessel with a pyramidal frustum shape and a liquid scintillator veto system. The fiducial decay volume is designed to detect two charged tracks, reconstructing vertices from dilepton and hadronic dark photon decays, followed by a spectrometer tracker and calorimeter.

(ii) The Forward Search Experiment at the High Luminosity LHC (FASER2) [36] is a proposed experiment designed to search for light, weakly interacting

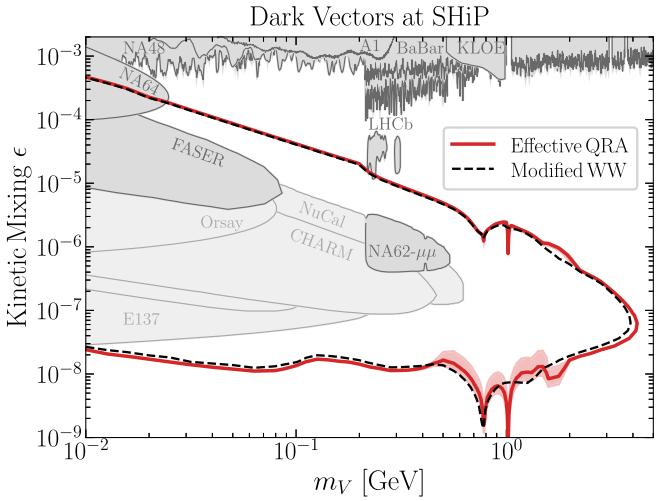


FIG. 8. Sensitivity reaches for dark vector decays at the SHiP experiment, comparing bremsstrahlung production via the effective QRA (solid red) with the modified WW approximation (dashed black), restricting the transverse momentum to $p_T < 4$ GeV following [113]. We incorporate various existing constraints along with the projections for SHiP and consider additional dark vector production modes, including meson decays following the BMPT [99] production distribution and the Drell-Yan process at higher mass [113].

particles such as dark photons. It will be situated within the Forward Physics Facility [63], approximately 620 meters downstream from the ATLAS interaction point, and will utilize the 14 TeV LHC beam with 3 ab^{-1} of integrated luminosity during the HL-LHC era. The FASER2 detector is compact, about 5 m long and 1 m in diameter, and is equipped with high-resolution silicon strip detectors for precise tracking and a calorimeter system with tungsten or lead absorbers for energy measurement. This relatively inexpensive detector features two veto stations with scintillator layers that detect coincident muon tracks to minimize muon-induced backgrounds. It is anticipated that timing information will allow for the complete elimination of these backgrounds in the experiment.

We focus on the visible decay of dark photons into lepton pairs and heavier hadronic states, such as $\pi^+\pi^-$. The expected event rates of dark photon searches for achieving the projected sensitivity reaches for each experiment are computed given the differential cross sections of all channels as shown in Fig. 5, convoluted with the survival or decay probability within the detector volume and considering the geometric acceptance of the detector. For SHiP, the vessel's acceptance probability ranges from 5% to 10%, depending on the dark photon production mode [113]. Reconstruction efficiency is near one for the bremsstrahlung channel but lower for meson decay channels due to the broader angular distribution of dark photons produced in these decays. A detailed discussion of these effects is beyond the scope of this paper, and we refer the reader to Refs. [113,115,116] for more information. Figures 7 and 8 indicate the resulting sensitivity contours compared to the earlier modified WW approach, making use of the FORESEE [112] package. Similar results can be obtained using SensCalc [70,117].

V. DISCUSSION

In this paper, we have refined the approach to modeling the forward production of dark vectors at proton colliders and fixed target experiments in the mass range from 0.5 to 2.0 GeV. Bremsstrahlung through ISR provides an important channel in this mass range, and we have improved the QRA approach to ISR via use of the Dawson correction to remove the unphysical $1/m_V^2$ singularity. This leads to a differential distribution (analogous to the one used for $q \to q'V$ for EW production in HERWIG) having kinematic features in common with the well-defined result for quasielastic radiation. We emphasize that the Dawson correction to the splitting function and the off-shell form factor at the $pp'V$ vertex are both important in obtaining a conservative estimate for dark photon ISR in which unphysical gauge-variant contributions are suppressed. We have also improved the analysis with a more complete treatment of the electromagnetic form factor at the proton vertex, including the dipole coupling, where resonant enhancements impact the sensitivity above the ρ/ω mass range. Fits to these form-factor contours are provided to enable straightforward implementation of this production model in other analyses [72].

We have also attempted to benchmark the dark vector production model by computing the analogous QRA rate for ρ meson production and comparing it with inclusive data from NA27. While the comparison is not one to one as there are additional production modes, it indicates that the QRA rate lies below the inclusive data for low radiated momenta as required.

The uncertainty in the form factors was parametrized to provide some indication of the precision of the overall QRA rate, which is necessarily lower for vector masses above the well-measured $\rho/\omega/\phi$ resonances. It is important to emphasize that this is just one source of uncertainty and the QRA approach has further limitations, due to the requirement of an on-shell treatment of the intermediate proton line. This does not allow for a rigorous test of gauge invariance at the vertex, beyond the use of the Dawson correction. While we have utilized various cross-checks to validate this approach in the restricted kinematic range that is most relevant for fixed target experiments, any extension to a broader range of kinematics would require further scrutiny. Thus, it is natural to ask how this analysis might be further improved. For fixed target experiments, the scattering of protons off target neutrons is also significant and could naturally be incorporated into the QRA analysis,

along with (kinematically softer) secondary production modes. There is also the important question of how to incorporate FSR contributions, which for fully inelastic processes would require at least a statistical treatment of hadronization or a full parton-level analysis. This may become feasible once parton distribution functions (PDFs) are sufficiently well constrained at small x.

Note added. Recently, related work was announced by Gorbunov and Kriukova [118,119], which has some overlap with the treatment of dipole form factors in Sec. III.

ACKNOWLEDGMENTS

We would like to express our thanks to F. Kling and M. Ovchynnikov for many helpful discussions and comments on the manuscript. We also thank M. Ovchynnikov for making us aware of the forthcoming analysis [70]. We are grateful to M. Hoferichter, A. Martínez Torres, and K. P. Khemchandani for helpful correspondence and assistance with the calculation of the dispersive form factors, and also to S. Dubnicka for assistance with the UA model code. S. F. and A. R. acknowledge the support of NSERC, Canada, and P. R. is supported by Fundação de Amparo à Pesquisa do Estado de São Paulo (FAPESP) under the Contract No. 2020/10004-7.

DATA AVAILABILITY

The data that support the findings of this article are openly available [72].

APPENDIX: NUCLEON ELECTROMAGNETIC FORM FACTORS

The nucleon electromagnetic form factors can be extracted from scattering data in the spacelike region ($t < 0$) and from the creation of nucleonantinucleon pairs in e^+e^- annihilation in the physical timelike region ($t > 4m_N^2$). However, we require knowledge of the form factor in the so-called unphysical timelike region $t \sim 1$ GeV^2 where data are missing, as indicated by the colored areas in Fig. 9, which therefore requires a model and/or careful spectral analyses. We will consider two approaches in this appendix.

In both approaches, the nucleon form factor is normalized,

$$F_1^p(0) = 1, \qquad F_1^n(0) = 0, \tag{A1}$$

$$F_2^p(0) = \mu_p - 1, \qquad F_2^n(0) = \mu_n, \tag{A2}$$

with $\mu_p = 2.793$ and $\mu_n = -1.913$ the magnetic moment of the proton and the neutron, respectively. At large momentum transfer, the asymptotic form of the Dirac and Pauli form factors is prescribed by perturbative QCD [120,121],

$$\lim_{t\to\infty} F_i(t) \sim \frac{1}{t^{i+1}}, \quad i = 1, 2, \tag{A3}$$

where logarithmic corrections [122] are neglected.

Experimental data are often presented in terms of the electric and magnetic Sachs form factors G_E and G_M, which are related to $F_{1,2}$ as follows (with N labeling the nucleon),

$$G_E^N(t) \equiv F_1^N(t) + \frac{t}{4m_N^2} F_2^N(t), \tag{A4}$$

$$G_M^N(t) \equiv F_1^N(t) + F_2^N(t). \tag{A5}$$

The timelike data are also presented in terms of the effective form factor

$$|G_{\text{eff}}^N| = \sqrt{\frac{|G_E^N|^2 + \xi |G_M^N|^2}{1+\xi}}, \tag{A6}$$

with $\xi = t/2m_N^2$ (see Ref. [92]). In the spacelike region, a successful method of determining the Sachs form factors has been the measurement of recoil polarizations that allows one to measure the ratio,

$$R_p \equiv \mu_p \frac{G_E^p}{G_M^p}. \tag{A7}$$

In this ratio, many systematic uncertainties cancel out, making this observable more robust than the Sachs form factors themselves, as indicated by gray data points in Fig. 9.

1. Unitary-analytic model

Unitarity implies that nucleon electromagnetic form factors are analytic functions throughout the entire complex t-plane, except for cuts extending along the positive real axis from the lowest continuum branch point t_0 to infinity. This property has been used to determine a UA template for the form factors with parameters determined via scattering data and knowledge of the vector-meson resonances. This UA model unifies the vector-meson pole contributions and effective cut structures [93]. The true neutral vector mesons—including $\rho(770)$, $\omega(782)$, $\phi(1020)$, $\rho(1450)$, $\omega(1420)$, $\phi(1680)$, $\rho(1700)$, $\omega(1650)$, and $\phi(2170)$ [123]—are combined in a series of poles within the framework of the VMD model, in the generic form

$$F(t) = \sum_{r=1}^{n} \frac{f_{V_r NN}}{f_{V_r}} \frac{m_{V_r}^2}{m_{V_r}^2 - t}, \tag{A8}$$

with the poles broadened, e.g., via the replacement $m_{V_r}^2 \to m_{V_r}^2 - i\Gamma_{V_r}/2$. The cut structures are implemented via a conformal mapping, which transforms the cut starting

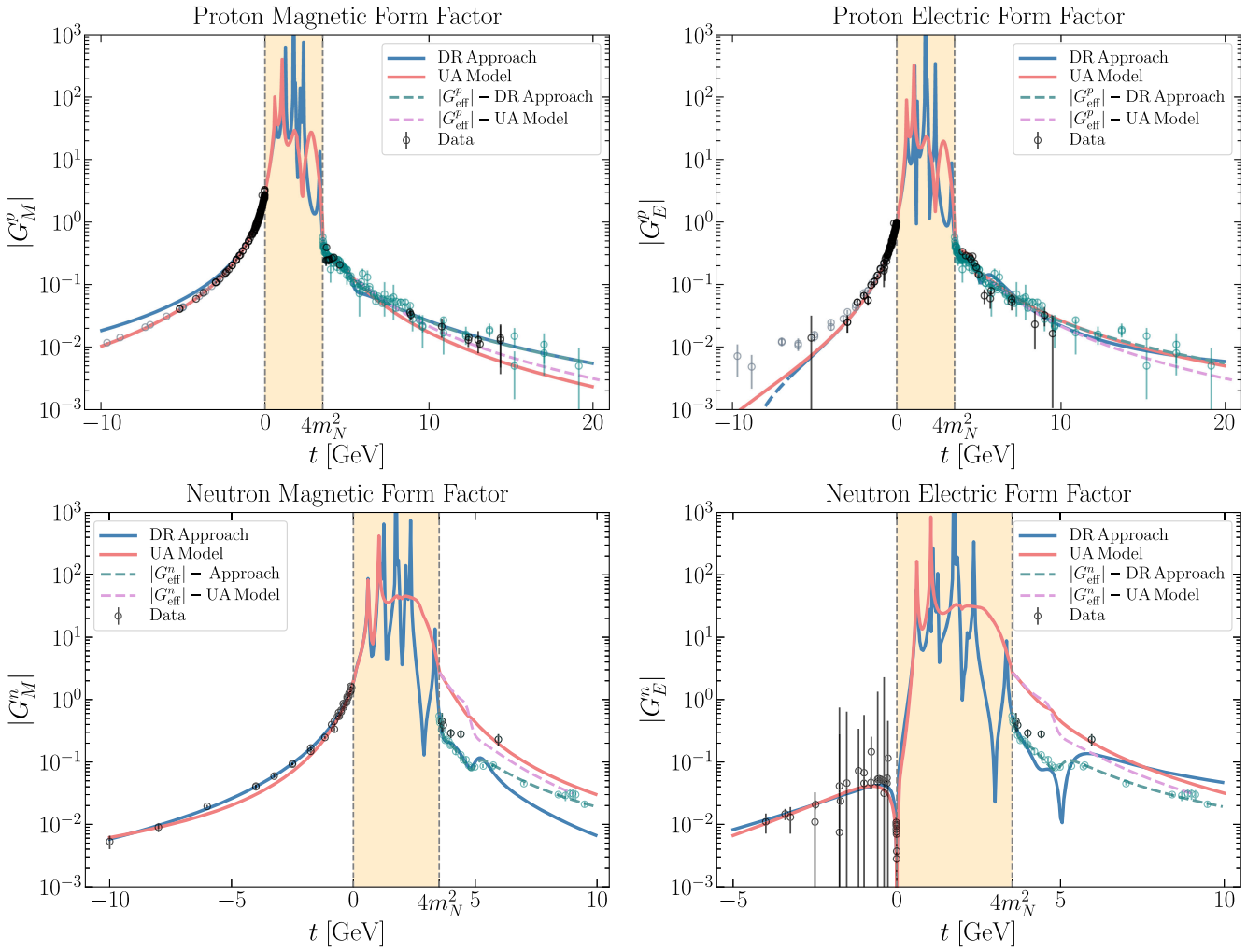


FIG. 9. Fit to the data for the electric and magnetic Sachs form factors of the nucleon using both the dispersion relation analysis (blue) and the unitary and analytic model (red) in both the spacelike and timelike regions. In the timelike region, the dashed lines represent G_{eff} from the dispersion relation analysis (green) and the unitary and analytic model (pink). The spacelike data for the proton (gray) at high Q^2 are uncorrected and excluded from the fit. See the text for further details.

at $t_{\text{cut}} = 4(9)m_\pi^2$ for the isovector (isoscalar) case in the t-plane onto the unit circle using a new variable,

$$V(t) = \frac{\sqrt{t_{\text{in}} - t_{\text{cut}}} - \sqrt{t_{\text{in}} - t}}{\sqrt{t_{\text{cut}} - t}}, \tag{A9}$$

with the corresponding inverse transformation taking the nonlinear form $t = t_{\text{cut}} + 4(t_{\text{in}} - t_{\text{cut}})V^2(t)/(V^2(t) - 1)^2$, where t_{in} parametrizes effective inelastic thresholds. This nonlinear transformation for t implies the relations $m_r^2 = t_{\text{cut}} + \frac{4(t_{\text{in}} - t_{\text{cut}})}{[1/V_r - V_r]^2}$ and $0 = t_{\text{cut}} + \frac{4(t_{\text{in}} - t_{\text{cut}})}{[1/V_N - V_N]^2}$, where $V_N = V(0)$ and $V_r = V(m_r^2)$. Applying these relations to Eq. (A8), the pole terms take the form

$$\frac{m_r^2 - 0}{m_r^2 - t} \to \left(\frac{1 - V^2}{1 - V_N^2}\right)^2 \left(\frac{(V_N^2 - V_r^2)(V_N^2 + 1/V_r^2)}{(V^2 - V_r^2)(V^2 + 1/V_r^2)}\right). \tag{A10}$$

Depending on the pole location relative to the effective inelastic threshold t_{in}, the introduction of a nonzero resonance width $m_r^2 \to (m_r^2 - i\Gamma_r/2)^2$ modifies the pole expression to $(1 - V^2)^2/(1 - V_N^2)^2 L_r(V)$, with L_r a complex function given in [93].

For the isoscalar and isovector Dirac and Pauli form factors, the values of t_{in} and the coefficients $\frac{f_{V_r NN}}{f_{V_r}}$ in the series (A8) are free parameters determined by comparing the model with existing data in spacelike and timelike regions simultaneously.

2. Dispersion relation analysis

In the dispersion relation (DR) approach [92,124,125], the spectral function $\text{Im}\, F(t)$ serves as the basic parametrization of physical effects contributing to the nucleon form factors. The general form of the spectral function permitted by unitarity consists of a combination of continua

and poles. The low-mass continua encompass 2π, $K\bar{K}$, and $\rho\pi$ contributions. Effective vector-meson poles are used to approximate higher-mass continua.

The complete isoscalar and isovector parts of the Dirac and Pauli form factors can then be parametrized as follows [124,126],

$$F_i^s(t) = F_i^{(s,K\bar{K})}(t) + F_i^{(s,\rho\pi)}(t) + \sum_{V=\omega,\phi,s_1,..} \frac{a_i^V}{m_V^2 - t},$$
$$F_i^v(t) = F_i^{(v,\pi\pi)}(t) + \sum_{V=v_1,v_2,..} \frac{a_i^V}{m_V^2 - t}, \tag{A11}$$

where $i = 1, 2$, and with poles again broadened, e.g., via the replacement $m_{V_r}^2 \to m_{V_r}^2 - i\Gamma_{V_r}/2$. The low-mass pole terms in (A11) correspond to physical vector mesons, namely, the $\omega(782)$ and the $\phi(1020)$, whereas the higher-mass poles ($s_1, s_2, \ldots$ for isoscalar and $v_1, v_2, \ldots$ for isovector channels) serve as effective parameters to account for unknown continuum contributions. The two-pion exchange continuum in the isovector form factor is derived using the pion form factor and the $\pi\pi \to N\bar{N}$ partial waves, which naturally exhibit the ρ-resonance along with a notable enhancement on the left shoulder of the resonance. We use the ancillary files of Ref. [126] for the isovector spectral functions, which include results from $\pi\pi \to N\bar{N}$ partial waves extracted from Roy-Steiner equations, consistent input for the pion vector form factor $F_\pi^V(t)$, and a discussion of isospin-violating effects.

The lowest isoscalar continuum, given by the 3-pion exchange, has been shown in chiral perturbation theory to be negligible such that there is no enhancement on the left wing of the ω resonance [127]. The next most important contributions are from $K\bar{K}$ and $\rho\pi$ continua, which can be represented by an effective pole term at the $\phi(1020)$ [125] and fictitious ω' meson with a mass $M_{\omega'} = 1.12$ GeV [128], respectively. Additional continua arising from a higher number of pions experience strong suppression. Given that the fit was already performed with the most up-to-date data sets, both in the spacelike and timelike regions, even including neutron data, we refrain from performing our analysis and use the fit results of Ref. [92].

The results of both the UA and DR approaches are compared to data in Fig. 9. While the fits are quite good in the spacelike and physical timelike domains, the two approaches diverge in the unphysical shaded region. We find that the UA model, constrained by the map to observed resonances, produces form factors that are somewhat lower overall; thus, to be conservative, we adopt this model in the rate analysis carried out in the paper.

[1] M. Pospelov, Secluded U(1) below the weak scale, Phys. Rev. D **80**, 095002 (2009).
[2] B. Batell, M. Pospelov, and A. Ritz, Probing a secluded U(1) at B-factories, Phys. Rev. D **79**, 115008 (2009).
[3] R. Essig, P. Schuster, and N. Toro, Probing dark forces and light hidden sectors at low-energy e+e- colliders, Phys. Rev. D **80**, 015003 (2009).
[4] M. Reece and L.-T. Wang, Searching for the light dark gauge boson in GeV-scale experiments, J. High Energy Phys. 07 (2009) 051.
[5] M. Freytsis, G. Ovanesyan, and J. Thaler, Dark force detection in low energy e-p collisions, J. High Energy Phys. 01 (2010) 111.
[6] B. Batell, M. Pospelov, and A. Ritz, Multi-lepton signatures of a hidden sector in rare B decays, Phys. Rev. D **83**, 054005 (2011).
[7] M. Freytsis, Z. Ligeti, and J. Thaler, Constraining the axion portal with $B \to Kl^+l^-$, Phys. Rev. D **81**, 034001 (2010).
[8] R. Essig, P. Schuster, N. Toro, and B. Wojtsekhowski, An electron fixed target experiment to search for a new vector boson A' decaying to e+e-, J. High Energy Phys. 02 (2011) 009.
[9] R. Essig, R. Harnik, J. Kaplan, and N. Toro, Discovering new light states at neutrino experiments, Phys. Rev. D **82**, 113008 (2010).
[10] K. L. McDonald and D. E. Morrissey, Low-Energy signals from kinetic mixing with a warped Abelian hidden sector, J. High Energy Phys. 02 (2011) 087.
[11] M. Williams, C. Burgess, A. Maharana, and F. Quevedo, New constraints (and motivations) for Abelian gauge bosons in the MeV-TeV mass range, J. High Energy Phys. 08 (2011) 106.
[12] S. Abrahamyan *et al.* (APEX Collaboration), Search for a new gauge boson in electron-nucleus fixed-target scattering by the APEX experiment, Phys. Rev. Lett. **107**, 191804 (2011).
[13] F. Archilli, D. Babusci, D. Badoni, I. Balwierz, G. Bencivenni *et al.*, Search for a vector gauge boson in phi meson decays with the KLOE detector, Phys. Lett. B **706**, 251 (2012).
[14] J. Lees *et al.* (*BABAR* Collaboration), Search for low-mass dark-sector Higgs bosons, Phys. Rev. Lett. **108**, 211801 (2012).
[15] H. Davoudiasl, H.-S. Lee, and W. J. Marciano, 'Dark' Z implications for parity violation, rare meson decays, and Higgs physics, Phys. Rev. D **85**, 115019 (2012).
[16] Y. Kahn and J. Thaler, Searching for an invisible A' vector boson with DarkLight, Phys. Rev. D **86**, 115012 (2012).
[17] S. Andreas, C. Niebuhr, and A. Ringwald, New limits on hidden photons from past electron beam dumps, Phys. Rev. D **86**, 095019 (2012).

[18] J. Alexander *et al.*, Dark sectors 2016 workshop: Community report, arXiv:1608.08632.
[19] M. Battaglieri *et al.*, US cosmic visions: New ideas in dark matter 2017: Community report, in U.S. Cosmic Visions: New Ideas in Dark Matter College Park, MD, USA, 2017 (2017), arXiv:1707.04591.
[20] J. Beacham *et al.*, Physics beyond colliders at CERN: Beyond the standard model working group report, J. Phys. G **47**, 010501 (2020).
[21] B. Batell, M. Pospelov, and A. Ritz, Exploring portals to a hidden sector through fixed targets, Phys. Rev. D **80**, 095024 (2009).
[22] P. deNiverville, M. Pospelov, and A. Ritz, Observing a light dark matter beam with neutrino experiments, Phys. Rev. D **84**, 075020 (2011).
[23] P. deNiverville, D. McKeen, and A. Ritz, Signatures of sub-GeV dark matter beams at neutrino experiments, Phys. Rev. D **86**, 035022 (2012).
[24] Y. Kahn, G. Krnjaic, J. Thaler, and M. Toups, DAEdALUS and dark matter, Phys. Rev. D **91**, 055006 (2015).
[25] C. Adams *et al.* (LBNE Collaboration), The long-baseline neutrino experiment: Exploring fundamental symmetries of the universe, arXiv:1307.7335.
[26] D. E. Soper, M. Spannowsky, C. J. Wallace, and T. M. P. Tait, Scattering of dark particles with light mediators, Phys. Rev. D **90**, 115005 (2014).
[27] B. A. Dobrescu and C. Frugiuele, GeV-Scale dark matter: Production at the main injector, J. High Energy Phys. 02 (2015) 019.
[28] P. Coloma, B. A. Dobrescu, C. Frugiuele, and R. Harnik, Dark matter beams at LBNF, J. High Energy Phys. 04 (2016) 047.
[29] P. deNiverville, C.-Y. Chen, M. Pospelov, and A. Ritz, Light dark matter in neutrino beams: Production modelling and scattering signatures at MiniBooNE, T2K and SHiP, Phys. Rev. D **95**, 035006 (2017).
[30] A. A. Aguilar-Arevalo *et al.* (MiniBooNE Collaboration), Dark matter search in a proton beam dump with MiniBooNE, Phys. Rev. Lett. **118**, 221803 (2017).
[31] A. A. Aguilar-Arevalo *et al.* (MiniBooNE DM Collaboration), Dark matter search in nucleon, pion, and electron channels from a proton beam dump with MiniBooNE, Phys. Rev. D **98**, 112004 (2018).
[32] J. Blümlein and J. Brunner, New exclusion limits on dark gauge forces from proton bremsstrahlung in beam-dump data, Phys. Lett. B **731**, 320 (2014).
[33] P. deNiverville, C.-Y. Chen, M. Pospelov, and A. Ritz, Light dark matter in neutrino beams: Production modelling and scattering signatures at MiniBooNE, T2K and SHiP, Phys. Rev. D **95**, 035006 (2017).
[34] J. L. Feng, I. Galon, F. Kling, and S. Trojanowski, ForwArd search ExpeRiment at the LHC, Phys. Rev. D **97**, 035001 (2018).
[35] C. Alpigiani *et al.* (MATHUSLA Collaboration), A letter of intent for MATHUSLA: A dedicated displaced vertex detector above ATLAS or CMS, arXiv:1811.00927.
[36] A. Ariga *et al.* (FASER Collaboration), Technical proposal for FASER: ForwArd Search ExpeRiment at the LHC, arXiv:1812.09139.
[37] B. Dutta, D. Kim, S. Liao, J.-C. Park, S. Shin, L. E. Strigari, and A. Thompson, Searching for dark matter signals in timing spectra at neutrino experiments, J. High Energy Phys. 01 (2022) 144.
[38] B. Batell, J. L. Feng, and S. Trojanowski, Detecting dark matter with far-forward emulsion and liquid argon detectors at the LHC, Phys. Rev. D **103**, 075023 (2021).
[39] B. Batell, J. L. Feng, A. Ismail, F. Kling, R. M. Abraham, and S. Trojanowski, Discovering dark matter at the LHC through its nuclear scattering in far-forward emulsion and liquid argon detectors, Phys. Rev. D **104**, 035036 (2021).
[40] J. D. Bjorken, R. Essig, P. Schuster, and N. Toro, New fixed-target experiments to search for dark gauge forces, Phys. Rev. D **80**, 075018 (2009).
[41] E. Izaguirre, G. Krnjaic, P. Schuster, and N. Toro, New electron beam-dump experiments to search for MeV to few-GeV dark matter, Phys. Rev. D **88**, 114015 (2013).
[42] M. D. Diamond and P. Schuster, Searching for light dark matter with the SLAC millicharge experiment, Phys. Rev. Lett. **111**, 221803 (2013).
[43] E. Izaguirre, G. Krnjaic, P. Schuster, and N. Toro, Physics motivation for a pilot dark matter search at Jefferson laboratory, Phys. Rev. D **90**, 014052 (2014).
[44] B. Batell, R. Essig, and Z. Surujon, Strong constraints on Sub-GeV dark sectors from SLAC beam dump E137, Phys. Rev. Lett. **113**, 171802 (2014).
[45] J. P. Lees *et al.* (*BABAR* Collaboration), Search for invisible decays of a dark photon produced in e^+e^- collisions at *BABAR*, Phys. Rev. Lett. **119**, 131804 (2017).
[46] A. Berlin, N. Blinov, G. Krnjaic, P. Schuster, and N. Toro, Dark matter, millicharges, axion and scalar particles, gauge bosons, and other new physics with LDMX, Phys. Rev. D **99**, 075001 (2019).
[47] D. Banerjee *et al.*, Dark matter search in missing energy events with NA64, Phys. Rev. Lett. **123**, 121801 (2019).
[48] A. Berlin, P. deNiverville, A. Ritz, P. Schuster, and N. Toro, Sub-GeV dark matter production at fixed-target experiments, Phys. Rev. D **102**, 095011 (2020).
[49] G. Krnjaic *et al.*, A snowmass whitepaper: Dark matter production at intensity-frontier experiments, arXiv:2207.00597.
[50] A. Berlin and F. Kling, Inelastic dark matter at the LHC lifetime frontier: ATLAS, CMS, LHCb, CODEX-b, FASER, and MATHUSLA, Phys. Rev. D **99**, 015021 (2019).
[51] M. Bauer, P. Foldenauer, and J. Jaeckel, Hunting all the hidden photons, J. High Energy Phys. 07 (2018) 094.
[52] A. Berlin, G. Krnjaic, and E. Pinetti, Reviving MeV-GeV indirect detection with inelastic dark matter, Phys. Rev. D **110**, 035015 (2024).
[53] C.-T. Lu, J. Tu, and L. Wu, Probing inelastic dark matter at the LHC, FASER, and STCF, Phys. Rev. D **109**, 015018 (2024).
[54] M. Mongillo, A. Abdullahi, B. B. Oberhauser, P. Crivelli, M. Hostert, D. Massaro, L. M. Bueno, and S. Pascoli, Constraining light thermal inelastic dark matter with NA64, Eur. Phys. J. C **83**, 391 (2023).
[55] A. Filimonova, S. Junius, L. Lopez Honorez, and S. Westhoff, Inelastic Dirac dark matter, J. High Energy Phys. 06 (2022) 048.

[56] M. Carrillo González and N. Toro, Cosmology and signals of light pseudo-Dirac dark matter, J. High Energy Phys. 04 (2022) 060.
[57] A. L. Foguel, P. Reimitz, and R. Z. Funchal, A robust description of hadronic decays in light vector mediator models, J. High Energy Phys. 04 (2022) 119.
[58] B. Batell, J. L. Feng, M. Fieg, A. Ismail, F. Kling, R. M. Abraham, and S. Trojanowski, Hadrophilic dark sectors at the forward physics facility, Phys. Rev. D **105**, 075001 (2022).
[59] G. D. V. Garcia, F. Kahlhoefer, M. Ovchynnikov, and T. Schwetz, Not-so-inelastic dark matter, J. High Energy Phys. 02 (2025) 127.
[60] P. A. Machado, O. Palamara, and D. W. Schmitz, The short-baseline neutrino program at Fermilab, Annu. Rev. Nucl. Part. Sci. **69**, 363 (2019).
[61] B. Abi *et al.* (DUNE Collaboration), Prospects for beyond the standard model physics searches at the deep underground neutrino experiment, Eur. Phys. J. C **81**, 322 (2021).
[62] M. Anelli *et al.* (SHiP Collaboration), A facility to search for hidden particles (SHiP) at the CERN SPS, arXiv: 1504.04956.
[63] J. L. Feng *et al.*, The forward physics facility at the high-luminosity LHC, J. Phys. G **50**, 030501 (2023).
[64] A. Celentano, L. Darmé, L. Marsicano, and E. Nardi, New production channels for light dark matter in hadronic showers, Phys. Rev. D **102**, 075026 (2020).
[65] F. Capozzi, B. Dutta, G. Gurung, W. Jang, I. M. Shoemaker, A. Thompson, and J. Yu, Extending the reach of leptophilic boson searches at DUNE and MiniBooNE with bremsstrahlung and resonant production, Phys. Rev. D **104**, 115010 (2021).
[66] N. Blinov, P. J. Fox, K. J. Kelly, P. A. N. Machado, and R. Plestid, Dark fluxes from electromagnetic cascades, J. High Energy Phys. 07 (2024) 022.
[67] P. Lo Chiatto and F. Yu, Consistent electroweak phenomenology of a nearly degenerate Z' boson, Phys. Rev. D **111**, 035001 (2025).
[68] W. Altmannshofer, J. A. Dror, and S. Gori, New opportunities for detecting axion-lepton interactions, Phys. Rev. Lett. **130**, 241801 (2023).
[69] D. Curtin, Y. Kahn, and R. Nguyen, Dark photons from charged pion bremsstrahlung at proton beam experiments, Phys. Rev. D **108**, 095039 (2023).
[70] Y. Kyselov and M. Ovchynnikov, Searches for long-lived dark photons at proton accelerator experiments, Phys. Rev. D **111**, 015030 (2025).
[71] S. Foroughi-Abari and A. Ritz, Dark sector production via proton bremsstrahlung, Phys. Rev. D **105**, 095045 (2022).
[72] See Supplemental Material at http://link.aps.org/supplemental/10.1103/fzlm-gsd7 providing numerical values for the Dirac and Pauli electromagnetic form factors of the proton in the timelike region, based on the Unitary and Analytic (UA) model used in this work. The first dataset contains the central values of the form factors as functions of the momentum transfer $\sqrt{(}t)$, while the second provides the corresponding uncertainty bands.
[73] P. Kessler, Sur une méthode simplifiée de calcul pour les processus relativistes en électrodynamique quantique, Nuovo Cimento (1955–1965) **17**, 809 (1960) [Nuovo Cimento (1955–1965) **17**, 809 (1960)].
[74] V. N. Baier, V. S. Fadin, and V. A. Khoze, Quasireal electron method in high-energy quantum electrodynamics, Nucl. Phys. **B65**, 381 (1973).
[75] V. N. Baier, E. A. Kuraev, V. S. Fadin, and V. A. Khoze, Inelastic processes in quantum electrodynamics at high-energies, Phys. Rep. **78**, 293 (1981).
[76] O. Nicrosini and L. Trentadue, Structure function approach to the neutrino counting problem, Nucl. Phys. **B318**, 1 (1989).
[77] G. Altarelli and G. Parisi, Asymptotic freedom in parton language, Nucl. Phys. **B126**, 298 (1977).
[78] A. K. Likhoded, A. V. Luchinsky, and A. A. Novoselov, Light hadron production in inclusive pp-scattering at LHC, Phys. Rev. D **82**, 114006 (2010).
[79] M. R. Masouminia and P. Richardson, Implementation of angularly ordered electroweak parton shower in Herwig 7, J. High Energy Phys. 04 (2022) 112.
[80] S. Dawson, The effective W approximation, Nucl. Phys. **B249**, 42 (1985).
[81] F. E. Low, Bremsstrahlung of very low-energy quanta in elementary particle collisions, Phys. Rev. **110**, 974 (1958).
[82] T. H. Burnett and N. M. Kroll, Extension of the low soft photon theorem, Phys. Rev. Lett. **20**, 86 (1968).
[83] V. Del Duca, High-energy bremsstrahlung theorems for soft photons, Nucl. Phys. **B345**, 369 (1990).
[84] D. Gorbunov and E. Kriukova, Dark photon production via elastic proton bremsstrahlung with non-zero momentum transfer, J. High Energy Phys. 01 (2024) 058.
[85] Y.-S. Liu and G. A. Miller, Validity of the Weizsäcker-Williams approximation and the analysis of beam dump experiments: Production of an axion, a dark photon, or a new axial-vector boson, Phys. Rev. D **96**, 016004 (2017).
[86] R. M. Davidson and R. Workman, Form-factors and photoproduction amplitudes, Phys. Rev. C **63**, 025210 (2001).
[87] G. Penner and U. Mosel, Vector meson production and nucleon resonance analysis in a coupled channel approach for energies $m_N < \sqrt{s} < 2$ GeV. II. Photon induced results, Phys. Rev. C **66**, 055212 (2002).
[88] A. Faessler, M. I. Krivoruchenko, and B. V. Martemyanov, Once more on electromagnetic form factors of nucleons in extended vector meson dominance model, Phys. Rev. C **82**, 038201 (2010).
[89] S. Okubo, Phi meson and unitary symmetry model, Phys. Lett. **5**, 165 (1963).
[90] G. Zweig, An SU(3) model for strong interaction symmetry and its breaking. Version 2, 10.17181/CERN-TH-412 (1964), pp. 22–101.
[91] J. Iizuka, Systematics and phenomenology of meson family, Prog. Theor. Phys. Suppl. **37**, 21 (1966).
[92] Y.-H. Lin, H.-W. Hammer, and U.-G. Meissner, New insights into the nucleon's electromagnetic structure, Phys. Rev. Lett. **128**, 052002 (2022).
[93] C. Adamuscin, E. Bartos, S. Dubnicka, and A. Z. Dubnickova, Numerical values of f^F, f^D, f^S coupling constants in $SU(3)$ invariant interaction Lagrangian of

vector-meson nonet with $1/2^+$ octet baryons, Phys. Rev. C **93**, 055208 (2016).
[94] J. J. Sakurai, Theory of strong interactions, Ann. Phys. (N.Y.) **11**, 1 (1960).
[95] N. M. Kroll, T. D. Lee, and B. Zumino, Neutral vector mesons and the hadronic electromagnetic current, Phys. Rev. **157**, 1376 (1967).
[96] T. D. Lee and B. Zumino, Field current identities and algebra of fields, Phys. Rev. **163** (1967) 1667.
[97] R. L. Workman *et al.* (Particle Data Group Collaboration), Review of particle physics, Prog. Theor. Exp. Phys. **2022**, 083C01 (2022).
[98] G. Antchev *et al.* (TOTEM Collaboration), First measurement of elastic, inelastic and total cross-section at $\sqrt{s} =$ 13 TeV by TOTEM and overview of cross-section data at LHC energies, Eur. Phys. J. C **79**, 103 (2019).
[99] M. Bonesini, A. Marchionni, F. Pietropaolo, and T. Tabarelli de Fatis, On particle production for high-energy neutrino beams, Eur. Phys. J. C **20**, 13 (2001).
[100] M. Aguilar-Benitez *et al.*, Inclusive particle production in 400-GeV/c pp interactions, Z. Phys. C **50**, 405 (1991).
[101] A. Suzuki *et al.*, High mass meson resonance production in pp interactions at 405-GeV/c, Nucl. Phys. **B172**, 327 (1980).
[102] E. Oset, Rho meson coupling to the nucleon in the chiral bag model, Conf. Proc. C **830821V2**, 625 (1983).
[103] C. Downum, T. Barnes, J. R. Stone, and E. S. Swanson, Nucleon-meson coupling constants and form-factors in the quark model, Phys. Lett. B **638**, 455 (2006).
[104] D. O. Riska and G. E. Brown, Nucleon resonance transition couplings to vector mesons, Nucl. Phys. **A679**, 577 (2001).
[105] E. Cortina Gil *et al.* (NA62 Collaboration), The beam and detector of the NA62 experiment at CERN, J. Instrum. **12**, P05025 (2017).
[106] B. Döbrich (NA62 Collaboration), Dark sectors at fixed targets: The example of NA62, Frascati Phys. Ser. **66**, 312 (2018),
[107] A. N. Diddens *et al.* (CERN-Hamburg-Amsterdam-Rome-Moscow Collaboration), A detector for neutral current interactions of high-energy neutrinos, Nucl. Instrum. Methods **178**, 27 (1980).
[108] Y.-D. Tsai, P. deNiverville, and M. X. Liu, Dark photon and muon $g-2$ inspired inelastic dark matter models at the high-energy intensity frontier, Phys. Rev. Lett. **126**, 181801 (2021).
[109] J. Blümlein *et al.*, Limits on neutral light scalar and pseudoscalar particles in a proton beam dump experiment, Z. Phys. C **51**, 341 (1991).
[110] A. Apyan *et al.*, DarkQuest: A dark sector upgrade to SpinQuest at the 120 GeV Fermilab Main Injector, in Snowmass 2021 (2022), 3, arXiv:2203.08322.
[111] S. Cerci *et al.*, FACET: A new long-lived particle detector in the very forward region of the CMS experiment, J. High Energy Phys. 06 (2022) 110.
[112] F. Kling and S. Trojanowski, Forward experiment sensitivity estimator for the LHC and future hadron colliders, Phys. Rev. D **104**, 035012 (2021).
[113] C. Ahdida *et al.* (SHiP Collaboration), Sensitivity of the SHiP experiment to dark photons decaying to a pair of charged particles, Eur. Phys. J. C **81**, 451 (2021).
[114] O. Aberle *et al.* (SHiP Collaboration), BDF/SHiP at the ECN3 high-intensity beam facility, Technical Report, CERN, Geneva, 2022, https://cds.cern.ch/record/2839677.
[115] A. Ariga *et al.* (FASER Collaboration), FASER's physics reach for long-lived particles, Phys. Rev. D **99**, 095011 (2019).
[116] H. Abreu *et al.* (FASER Collaboration), Search for dark photons with the FASER detector at the LHC, Phys. Lett. B **848**, 138378 (2024).
[117] M. Ovchynnikov, J.-L. Tastet, O. Mikulenko, and K. Bondarenko, Sensitivities to feebly interacting particles: Public and unified calculations, Phys. Rev. D **108**, 075028 (2023).
[118] D. Gorbunov and E. Kriukova, Pauli form factor contributions to the inelastic proton bremsstrahlung and dark photon production, J. High Energy Phys. 02 (2025) 018.
[119] D. Gorbunov and E. Kriukova, Dark photon production via inelastic proton bremsstrahlung with Pauli form factor, Phys. Part. Nucl. **56**, 506 (2025).
[120] S. J. Brodsky and G. R. Farrar, Scaling laws for large momentum transfer processes, Phys. Rev. D **11**, 1309 (1975).
[121] G. P. Lepage and S. J. Brodsky, Exclusive processes in perturbative quantum chromodynamics, Phys. Rev. D **22**, 2157 (1980).
[122] A. V. Belitsky, X.-d. Ji, and F. Yuan, A perturbative QCD analysis of the nucleon's Pauli form-factor $F_2(Q^2)$, Phys. Rev. Lett. **91**, 092003 (2003).
[123] C. Patrignani *et al.* (Particle Data Group), Review of particle physics, Chin. Phys. C **40**, 100001 (2016).
[124] Y.-H. Lin, H.-W. Hammer, and U.-G. Meissner, Dispersion-theoretical analysis of the electromagnetic form factors of the nucleon: Past, present and future, Eur. Phys. J. A **57**, 255 (2021).
[125] M. A. Belushkin, H. W. Hammer, and U. G. Meissner, Dispersion analysis of the nucleon form-factors including meson continua, Phys. Rev. C **75**, 035202 (2007).
[126] M. Hoferichter, B. Kubis, J. Ruiz de Elvira, H. W. Hammer, and U. G. Meissner, On the $\pi\pi$ continuum in the nucleon form factors and the proton radius puzzle, Eur. Phys. J. A **52**, 331 (2016).
[127] V. Bernard, N. Kaiser, and U.-G. Meissner, Nucleon electroweak form-factors: Analysis of their spectral functions, Nucl. Phys. **A611**, 429 (1996).
[128] U.-G. Meissner, V. Mull, J. Speth, and J. W. van Orden, Strange vector currents and the OZI rule, Phys. Lett. B **408**, 381 (1997).